Momentum- and space-resolved high resolution electron energy loss spectroscopy of individual single wall carbon nanotubes

F.S. Hage[1,*], T. P. Hardcastle[1,2], A.J. Scott[2], R. Brydson[2], Q.M. Ramasse[1,*]

[1]SuperSTEM Laboratory, SciTech Daresbury Campus, Daresbury, WA4 4AD, UK.

[2]School of Chemical and Process Engineering, University of Leeds, Leeds, LS2 9JT, UK.

[*]Email: fshage@superstem.org; qmramasse@superstem.org

The ability to probe the electronic structure of individual nano-objects at high energy resolution using momentum- and spatially-resolved electron energy loss spectroscopy in the scanning transmission electron microscope is demonstrated through the observation of confinement of the π plasmon in individual single wall carbon nanotubes. While confinement perpendicular to the tube axis was identified for all investigated tubes, a variable degree of confinement parallel to the tube axis was attributed to the concentration of topological defects. Spatially-resolved valence loss spectra allowed for the identification of a loss peak attributed to a chirality-dependent radial interband transition. Furthermore, the importance of a careful consideration of loss peak momentum dispersions for the interpretation of spatially resolved valence loss spectra is discussed.

I. INTRODUCTION

18   Since 1991, the interest in carbon nanotubes (CNTs)[1] has remained high in the scientific community. This is in

19   part due to the wide range of electronic properties (from semi-conducting to metallic) that single wall (SW)

20   CNTs can exhibit [2]. The electronic properties of a SWCNT are to a large degree determined by its chirality,

21   which is commonly described by a set of chiral indices (n, m).[3] A SWCNT of a given (n, m) set of indices will

22   exhibit sharp non-smooth peaks in the quasi-1D valence and conduction band density of states (DoS), referred to

23   as van Hove singularities (vHSs). Scanning tunnelling spectroscopy (STS) allows for direct probing of the

24   density of states (DoS) of individual SWCNTs suspended in vacuum, however, STS measurements are

25   reportedly afflicted by substrate effects.[4] Transitions between the sharp vHS peaks in the valence and

26   conduction band have been reported using a range of techniques including electron energy loss spectroscopy

27   (EELS) using a purpose-built stand-alone spectrometer apparatus,[5-8] Rayleigh scattering spectroscopy (RSS),[9, 10]

28   fluorescence excitation spectroscopy[11], optical absorption spectroscopy[12] and spatial modulation (optical)

29   spectroscopy (SMS).[13, 14] While most of these methods lack the spatial resolution to investigate individual

30   CNTs, measurements have been reported for individual suspended SWCNTs using STS[4], RSS[10] and SMS.[13]

31   Due to recent advancements in transmission electron microscope (TEM) electron source monochromation,[15-17]

32   an EEL spectrometer coupled to a TEM column now allows for detailed investigations of $\pi \rightarrow \pi^*$ transitions

33   between the SWCNT conduction and valence vHSs.[18, 19] Moreover, TEM and scanning (S)TEM allow for the

34   determination of the chiral indices of each investigated tube using either a Fourier transform (FFT) of a high

35   resolution image[19, 20] or an electron diffraction pattern.[18, 21, 22] Note that the CNT valence loss spectrum (EEL<

36   50 eV) does not only contain peaks corresponding to chirality dependent $\pi \rightarrow \pi^*$ transitions but also provides

37   information about higher energy interband transitions involving σ states, as well as two collective modes of the

38   system: the π and $\pi+\sigma$ plasmons. The dispersion of both inter-band transitions and collective modes across the

39   Brillouin zone can be investigated by resolving valence loss spectra in momentum space. Indeed, SWCNT

40   "bulk" or ensemble measurements (*i.e.* averaged over samples containing a large number of SWCNTs to

41   measure) using a purpose-built stand-alone spectrometer apparatus have shown that the collective π valence

42   electron response comprises a non-dispersive (π_1) and dispersive (π_2) mode.[6-8] The π_1 plasmon exhibits a

43   vanishing dispersion which has been attributed to plasmon confinement perpendicular to the CNT axis,[5-8] while

44   the distinct dispersion of the π_2 plasmon has been interpreted in terms of a plasmon propagating along the CNT

45   axis.[6-8] This can be understood from the freedom to vary the wave vectors continuously along the unconfined

46 length of the tube which allows for modes of varying momentum, with no such freedom appearing for modes

47 perpendicular to the CNT axis, where allowed wave vectors are restricted to a limited number of chirality

48 dependent values within a discrete set (see *e.g.* [23]). Momentum-resolved EELS of related carbon materials has

49 been reported using TEM (graphene)[24-26] and STEM (individual multilayer graphene nanocones).[27]

50 The present work is focused on taking advantage of the combined spatial and energy resolution of a state-of-the-

51 art monochromated STEM-EELS system to investigate the valence loss response of individual SWCNTs in real

52 and momentum space. While momentum resolved STEM-EELS of the carbon K ionisation edge has been used

53 to map defects in individual multiwalled CNTs,[28] to the knowledge of the authors, the present work is the first

54 report on plasmon dispersions acquired from individual SWCNTs using EELS. In contrast to methods where the

55 spectroscopic signal is acquired from SWCNT "bulk samples",[5-8] STEM-EELS allows uniquely for the

56 characterisation of the electronic structure and plasmon dispersions as a function of both the chirality of

57 individual SWCNTs and the possible presence of (atomic-sized) defects in the tubes. The present results

58 confirm that π plasmon confinement perpendicular to the CNT axis occurs for individual tubes. Moreover, an

59 observed variable π plasmon confinement parallel to the tube axis is attributed to the concentration of

60 topological defects present in the individual SWCNTs probed here. Specifically, these topological defects are

61 non-hexagonal rings incorporated in the SWCNT walls. Intriguingly, the topological-defect-induced collective

62 mode confinement appeared to predominantly affect the π valence electrons. This can be rationalised in terms of

63 non-hexagonal ring defects disrupting the delocalised π states along the tube axis, which in turn affects the

64 collective response of the π valence electrons. As σ states are significantly more localised than π states, the lack

65 of an observed confinement of the collective response of the σ valence electrons may be explained by σ states

66 being much less susceptible to isolated atomic scale defects than π states. Whilst the exact mechanism through

67 which topologically-induced π plasmon confinement occurs has yet to be determined, it is suggested that the

68 role of topological defects in CNTs, and by extension graphene, should be taken into consideration in the

69 development of any novel CNT- or graphene-based plasmonic and opto-electronic devices. Moreover, it is

70 proposed that topological defect engineering could be used to form plasmonic conduits and possibly more

71 complex functional geometries in graphene. The present results highlight the advantage of combining spatially-

72 and momentum-resolved valence EELS measurements. Recorded loss peak dispersions across the Brillouin zone

73 were in particular crucial in developing a coherent interpretation of $\pi+\sigma$ plasmon peak fine structure as a

74 function of distance to the nanotube axis, as well as for the assignment of a loss peak for a (13,7) metallic

75 SWCNT as a radial chirality-dependent interband transition.

II EXPERIMENTAL DETAILS

STEM-EELS experiments were carried out using a Nion UltraSTEM100MC monochromated dedicated STEM, equipped with a Gatan Enfinium ERS spectrometer optimised for high-stability. The microscope was operated at an acceleration voltage of 60 kV. The spatially resolved valence loss spectra in Figs. 2, 3 and 8 were acquired with a convergence semi-angle (α) of 31 mrad (1.0 Å probe size) and a spectrometer collection semi-angle (β) of 44 mrad. C-K core loss spectra in Fig. 2 were acquired with α=31 mrad, β=60 mrad. Momentum-resolved spectra shown in Figs. 5 and 6 were acquired using a "nano-diffraction mode", *i.e.* a small, mostly parallel probe with residual convergence of $\alpha = 0.9$ mrad, yielding an estimated diffraction-limited probe size of ~ 3 nm. In Fig. 1, the medium angle annular dark field (MAADF) images were acquired with $\alpha = 31$ mrad, while the diffraction patterns were acquired using the "nano-diffraction" mode ($\alpha = 0.9$ mrad).

The momentum selectivity of the valence loss spectra was achieved by modifying the post-specimen lens excitations as well as limiting the spectrometer acceptance angle with a rectangular spectrometer entrance slit (see *e.g.* Refs. [24, 25]). The slit was oriented in such a way that the narrow part of the slit was parallel to the energy dispersive direction of the spectrometer. This results in a two-dimensional spectrum forming on the spectrometer camera, where the wave vector and EEL axes are perpendicular. This means all momentum-resolved spectra were acquired in parallel, instead of serially (see *e.g.* Refs. [27, 29]). Individual spectra were extracted from the full dataset along the "wave vector axis", at an increment of the effective pixel size $\Delta q_q = 0.06$ Å^{-1}. From adding the angular spread of the electron beam $2\alpha = 0.22$ Å^{-1} and the effective slit width $\Delta q_{EEL} = 0.48$ Å^{-1} in quadrature, the momentum resolution was estimated to be $\Delta q \approx \pm 0.25$ Å^{-1}.

The energy resolution, measured as the full-width at half-maximum of the quasi-elastic zero loss peak (ZLP), was 60 meV for the spatially resolved measurements and 80-120 meV for the momentum-resolved measurements, at a dispersion on the spectrometer camera of 20 meV per channel where $\alpha = 31$ mrad and $\alpha = 0.9$ mrad, respectively. This difference in energy resolution is attributed mostly to an increase in uncorrected chromatic spectrometer aberrations accompanying the change in post specimen lens setup going from the "spatially resolved" to the "momentum resolved" beam geometry. C-K ionisation edges in Fig. 2 were averaged across the tube diameters and acquired with an effective energy resolution of 150 meV, at a dispersion of 50 meV per channel. The C-K edges were calibrated to a nominal onset of the π^* peak at 284 eV. Peak values in Tables II, III and in the plots in Fig. 7 were determined by Gaussian fitting of background-subtracted spectra. The uncertainties of the measured energy loss values in Fig. 7 are primarily attributed to choice of fitting

4

105   function and fitting parameters, the magnitude of which is expected to increase with the degree of peak overlap

106   and increasing spectral noise (in practice with increasing q). Precisely determining these errors is problematic in

107   the present case; however an estimate was achieved by measuring peak values from the extremes of acceptable

108   fits for a select number of representative spectra over the entire measured momentum range, for all three tubes.

109   The resulting non-standard errors range from $< \pm 0.02\,\mathrm{eV}$ at low q to a maximum of $\sim \pm 0.2\,\mathrm{eV}$ for the highest

110   q measurements.

111   In Figs. 2-6, and 8, the spectral background was subtracted using a power law, except for the (13,7) tube in Figs.

112   5 and 6 where a 1st order polynomial model was used. The 1st order polynomial model was likely required for

113   adequate background subtraction in order to compensate for un-resolved $\pi \rightarrow \pi^*$ contributions to the ZLP tail of

114   the metallic tube spectra. Commercially-available powders of SWCNTs (produced through laser ablation) were

115   dispersed onto standard lacy carbon TEM support films after sonication in ethanol. The grid was heated to 130

116   °C in vacuum (pressure below 5x10^{-5} Torr) prior to insertion into the microscope vacuum in order to prevent

117   contamination build-up (extraneous hydrocarbons) which would otherwise risk covering the CNTs.

III RESULTS AND DISCUSSION

A. SWCNT chirality and defects

120   Fig. 1 shows diffraction patterns and MAADF STEM images of three tubes whose chiral indices were assigned

121   to be (15,10), (15,1) and (13,7), as discussed below. Note that the orientation of the tubes in the MAADF images

122   is not directly related to the orientations of the diffraction patterns. A SWCNT can be classified as either

123   semiconducting or metallic based on its chiral index (n, m): a tube is metallic if 2n+m=3N (where N is an

124   integer); otherwise the tube is semiconducting.[30] Thus the (15,10) and (15,1) tubes are semiconducting while the

125   (13,7) tube is metallic. MAADF images in Fig. 1 clearly show that the tubes are single-walled, and, in the case

126   of the (15,1) tube, clean and defect free. The (15,10) and (13,7) tubes are both sparsely covered by or containing

127   thin layers of disordered carbonaceous material, appearing as brighter contrast regions in the MAADF images

128   (Fig. 1). While likely primarily carbon-based, this disordered material could possibly also contain a smaller

129   amounts of other elements originating from the CNT production process. A detailed study of the carbonaceous

130   material elemental composition was however beyond the scope of the present work. Moreover, the white

131   arrows in the images in Fig. 1 indicate the presence of topological defects in both the (15,10) and (13,7) tubes.

132   Specifically, Fig.1 indicates that the topological defects are primarily non-hexagonal rings (see white arrows,

133   Fig.1) incorporated the in the graphene sheets making up the walls of the CNTs. Contributions of tube

134   imperfections to the recorded loss spectra will be discussed below.

135   Table I shows the chiral angles, ratio of chiral indices (m/n) and individual chiral indices determined from the

136   SWCNT diffraction patterns in Fig. 1, following Refs.[21, 22]. Ratios between the position of the first and second

137   diffraction peak of the so-called principal layer lines in a SWCNT diffraction pattern, denoted X_2/X_1, can be

138   used to assign chiral indices directly.[22] The precision of all values extracted from the diffraction patterns was

139   however limited by a combination of a finite electron beam convergence and camera dynamic range. Due to

140   these uncertainties and sources of noise, additional information was therefore used to confirm the chiral

141   assignment.

142   The carbon K edge π^* peak fine structure is dominated by transitions from the 1s ground state to vHSs in the

143   unoccupied DoS above the Fermi level, thus is highly sensitive to tube chirality.[19, 31] This has been

144   demonstrated experimentally for individual SWCNTs using (S)TEM-EELS by Rossouw et al.[31] and Senga et

145   al.[19] Rossouw et al.[31] showed that the π^* peak exhibits significantly different line shapes depending on whether

146   an individual tube is metallic and semi-conducting. Senga et al.[19] investigated several individual metallic and

147   semi-conducting tubes, demonstrating that the π^* peak fine structure is significantly affected by tube chirality.

148   Upon detailed analysis, they found excellent agreement between experimental π^* peak fine structure and tight

149   binding calculations.[19] Thus, it is clear that the C-K π^* peak fine structure can allow for detailed analysis of the

150   chirality dependent unoccupied DoS of individual SWCNTs. In the present case, Fig. 2 shows core loss spectra

151   from the (15,10), (15,1) and (13,7) tubes. The π^* fine structure in Fig. 2 clearly varies significantly with tube

152   chirality. Upon comparison to literature, the (13,7) tube π^* fine structure appears similar to that observed for

153   metallic tubes in Refs.[19, 31], while the (15,1) and (15,10) tube π^* fine structures show similarities to semi-

154   conducting tubes in Ref.[19] and Refs.[19, 31], respectively. A more detailed analysis of the spectra in Fig. 2 was

155   beyond the scope of the present work. In a more general perspective, SWCNT C-K π^* peak fine structure

156   analysis with a view to determine chirality directly could in some cases possibly be complicated due to factors

157   such as limited experimental spectral resolution, lifetime broadening[19, 32] and relatively small energy separations

158   between conduction band vHSs for some tubes. Nevertheless, in comparison to valence loss spectra (discussed

159   below), the recorded C-K edge signal is highly localised,[19, 32, 33] so that no effect from topological defects or

160   superimposed disordered material $\geq$ 1 nm away is expected to influence the EEL spectrum, which presents an

161   advantage over valence loss based assignment techniques for the analysis of local SWCNT electronic structure.

6

162   Fig. 3 shows valence loss spectra acquired from each tube with the electron beam incident on the centre of the

163   tube, indicated by the white discs in Fig. 1. Tables II and III compare $\pi \rightarrow \pi^*$ vHS peak positions for the spectra

164   in Fig. 3 to literature values obtained from Rayleigh scattering spectroscopy,[9, 10] fluorescence excitation

165   spectroscopy,[11] interpolation from experimental data,[9] optical absorption spectroscopy[12] and a prediction based

166   on fluorescence data.[34] In agreement with Sato and Terauchi[18] the $\pi \rightarrow \pi^*$ vHS EELS peaks appear at up to ≈ 0.2

167   eV higher energy than those measured by optical techniques. While the EEL spectrum is proportional to the loss

168   function, the optical absorption spectrum is given by the imaginary part of the dielectric function (see *e.g.* Ref.

169   [35]). Thus the observed vHS EELS peak values can be rationalised by the contribution of the real part of the

170   dielectric function to the loss function:[32, 36] effectively shifting vHS EELS peaks away from the corresponding

171   optical values (given by maxima in the imaginary part of the dielectric function).

172   The nomenclature for assigning $\pi \rightarrow \pi^*$ transitions between vHSs in the valence loss spectrum follows that of

173   refs.[18, 19, 37] While, to the knowledge of the authors, experimental literature values confirming the energies of the

174   (15, 10) $E_{55} - E_{77}$ and (15,1) $E_{33} - E_{66}$ peaks are lacking, these peaks were tentatively assigned to transitions

175   between higher energy vHSs, as this is their most likely origin. Alternatively, assignment as "vHS peaks" might

176   be done on the basis of theoretical modelling;[18] however this was beyond the scope of the present study.

177   Due to the so-called trigonal warping effect[23] there is a splitting of the equivalent M_{11} and M_{22} vHS peaks

178   typically observed in metallic CNTs. The splitting is reflected in nomenclature where M_{11}^- and M_{11}^+ (resp. M_{22}^-

179   and M_{22}^+) corresponds to the lower (-) and higher energy (+) vHSs EEL peak. The magnitude of vHS peak

180   splitting is chirality dependent.[23] Here, a clear splitting of the M_{22} peak can be observed, whereas the splitting is

181   not as pronounced for the M_{11} peak, even though for (13,7) SWCNTs, a 0.13-0.15 eV splitting of the M_{11} peak

182   has been reported by optical measurements.[9, 12] The lack an obvious splitting of the M_{11} peak in the (13,7) tube

183   EEL spectrum in Fig. 3(a) is attributed to experimental factors: predominantly spectral noise and obfuscation by

184   the intense tail of the ZLP. Overall, by comparing experimentally-measured structural parameters and valence

185   vHS peak energies to reported values[9-12, 22, 34] as summarised in Tables I-III, as well as comparison of the C-K

186   core-loss fine structures to literature,[19, 31] it was possible to unambiguously confirm the chirality assignment of

187   the three SWCNTs in Fig. 1.

B. Low loss EELS features in SWCNTs

189   In addition to "vHS" $\pi \rightarrow \pi^*$ peaks, the loss spectra in Fig. 3 exhibit further features at ≈ 4.9-5.0 eV, ≈ 13.7-9 eV

190   and ≈ 15.6-15.8 eV, which are attributed to the π plasmon,[5-7, 38] a sum over interband transitions (IB)[6, 7] and the

7

191   π+σ plasmon, respectively.[5-7, 38] Plasmon peaks can be understood as arising from the incident electron beam

192   setting up a collective oscillation including only the π or all (π+σ) valence electrons.[39] In a first approximation

193   the "IB peak" might be attributed to a sum over σ→σ* transitions.[35, 40, 41] This assignment assumes that the

194   recorded spectrum is dominated by the $q\rightarrow0$ tangential response. However, due to tube wall curvature and the

195   use of a finite spectrometer collection aperture, additional contributions to the IB loss peak from σ→π* and

196   π→σ* transitions are expected. While diameter dependent[40] and possibly other chirality-induced effects might

197   be expected for EEL >10 eV, qualitatively the IB peaks appear highly similar in all three spectra in Fig. 3. This

198   might in part be due to the more intense π+σ peak obscuring any IB peak fine structure.

199   Due to so-called inelastic delocalisation,[32] valence loss spectra record information from inelastic energy losses

200   occurring up to several nm away from the position of the electron probe. A varying proximity of the electron

201   beam (whose placement is indicated by the white discs in Fig. 1) to tube imperfections, such as topological

202   defects and covering disordered carbonaceous material, allows for a comparison of the contribution of these

203   imperfections to the spectra in Fig. 3. Any such effect will take the form of contributing spectral features

204   characteristic of disordered carbon[42] and topological defects,[43-45] that increases in relative intensity with

205   increasing proximity to the electron beam position,[32] which if present, must be taken into account in any detailed

206   analysis. However, when comparing the spectra of the three tubes there are no apparent < 5 eV inter-band

207   transition peaks in the (15,10) and (13,7) spectra that unambiguously could be assigned to topologically-induced

208   electron structure modification.[43-45] Such peaks are likely to arise due to excitations between defect states close

209   to the Fermi level,[43] the intensity of which should increase with increasing proximity of the electron beam to the

210   defects in question. The present results are in agreement with the results of Senga et al.[19] who did not observe

211   any additional contribution due to tube defects in this energy range. In terms of disordered carbonaceous

212   material contribution, Fig. 4 shows there is a small increase in the shoulder of the π+σ peak of the (13,7) tube

213   spectrum at $\geq \sim 20\,eV$ as compared to the (15,1) and (15,10) tube spectra. This can be attributed to a minor

214   contribution of the 22-23 eV π+σ plasmon of disordered carbon,[42] rather than to any dependence on chirality or

215   on the presence of topological defects. Overall, the spectra in Fig. 3 therefore show no distinct features

216   characteristic of tube modification in proximity to the electron probe for energy losses $< \sim 20\,eV$.

217   In the recent work of Senga et al.,[19] spectra acquired from metallic tubes exhibited a peak at ~ 1eV that the

218   authors attributed to the SWCNT free charge carrier plasmon, the origin of which is the collective excitation of

219   free charge carriers in metallic or doped semi-conducting SWCNTs, that propagate along the nanotube axis.

220 The charge carrier plasmon energy is affected by both finite CNT diameter,[46] length, and charge carrier

221 density,[47, 48] however, the exact origin of the CNT (and graphene) charge carrier plasmon is reportedly a subject

222 of some debate in the scientific community.[48] The charge carrier plasmon, attributed to collective excitation of

223 the free charge carriers near the Fermi level, is thus distinctly different from the π and $\pi+\sigma$ plasmons, which are

224 attributed to the collective excitation of the π, and, a combination of π and σ valence electrons, respectively.

225 Intriguingly, no charge carrier plasmon peak was observed for the (13,7) tube either in the present work or for

226 the metallic tubes investigated by Sato and Terauchi.[18] In the present work, distinct spectral features are clearly

227 resolved down to 0.97 and 0.79 eV for the (15,1) and (15,10) tubes in Fig. 3, respectively, indicating that the

228 experimental conditions would have allowed for the detection of such a feature at ~ 1eV, if present. Moreover,

229 the absence of the charge carrier plasmon peak in the present case cannot be explained solely by differences in

230 momentum resolution, which would have a determining effect on its visibility, as the spectra in Fig. 3 were

231 acquired at a momentum resolution that is comparable to that used by Senga et al.[19] The absence of an

232 observable charge carrier plasmon peak for the (13,7) tube might thus be explained either by the (13,7) charge

233 carrier plasmon peak having a much lower relative intensity than the peaks identified by Senga et al.[19] (due to an

234 undetermined dampening mechanism specific to the specific tube observed here) or by the energy of the peak

235 appearing at an energy loss below the resolution of the experiment for the (13,7) tube. The latter seems the most

236 likely explanation: the charge carrier plasmon was reported in the literature to shift from 0.9 eV to 0.6 eV in a

237 single defective (12,3) SWCNT, when the electron beam is moved $\approx$ 4 nm from a defect-free region to a region

238 where topological defects are present.[19] In the present case the electron beam is in relatively close proximity to a

239 section with a higher concentration of topological defects (minimum distance of 3.2 nm, see Fig. 1), which

240 might explain a possible peak value of < 0.79 eV. Moreover, Senga et al.[19] suggested that unintentional doping

241 by the TEM support grid might explain the relatively high charge carrier plasmon peaks peak observed for the

242 metallic tubes they investigated. If in the present case the degree of a possible "unintentional doping" is

243 significantly smaller, this could also explain why the (13,7) tube charge carrier plasmon could appear at an EEL

244 < 0.79 eV. Clearly detailed studies using monochormated STEM-EELS might significantly improve the

245 understanding of how the charge carrier plasmon of individual SWCNTs might be affected by tube defects and

246 doping, as well as nanotube length[47, 48] and diameter.[46] While a detailed study of charge carrier plasmons in

247 individual carbon nanotubes would likely be of significant interest to the scientific community, this is beyond

248 the scope of the present work.

249

C. Momentum resolved valence loss spectra

251 The momentum dependence of the observed SWCNT loss modes can be seen in Figs. 5 and 6, with fitted peak

252 values shown in Fig. 7. The direction of q with respect to the CNT axial direction for each tube is indicated in

253 the diffraction patterns in Fig. 1. Spectra from all three tubes show a dispersive π+σ peak (*i.e.* its energy changes

254 with momentum) that broadens with increasing q and a non-dispersive IB peak that becomes indistinguishable

255 from noise for $q \geq 0.6 - 0.7 \, \text{Å}^{-1}$. As the momentum-resolved spectra were acquired in parallel, and because

256 the spectrometer camera has a finite dynamic range, the spectral intensity q^{-2} dependence[39] necessarily results

257 in spectral noise increasing significantly with increasing q. This can clearly be seen in Figs. 5 and 6. While Figs.

258 5 and 6 show smoothed spectra as a guide to the eye, the loss mode identification (Figs. 5, 6) and peak fitting

259 (Fig. 7) were carried out using the otherwise-unprocessed background-subtracted data, in order to avoid any

260 potential artefact introduced by processing.

261 Qualitatively the π→π* peaks resolved in Fig. 5 appear to be non-dispersive for the (15,10) and (15,1) tubes, in

262 agreement with the literature.[5, 49] However, significant spectral noise made the unambiguous determination of

263 their dispersion from the spectra in Fig. 5 problematic. For the (13,7) tube, a lack of observable π→π* peaks for

264 the momentum-resolved spectra is attributed to a combination of spectral noise and obscuring by the ZLP tail

265 having increased as compared to the spectra in Fig. 3 due to a relative decrease in effective energy resolution

266 (see section II).

267 The (15,10) and (15,1) tubes demonstrate arguably the most intriguing feature of these momentum-resolved

268 spectra with a clear splitting of the π plasmon peak into a non-dispersive π_1 and a dispersive π_2 mode. While the

269 π peak split is identifiable in Fig. 5, this is perhaps easier to observe unambiguously in Fig. 6, which shows

270 spectra for selected momentum transfers over a limited energy loss range. The π_1 mode is present in all three

271 tubes, but the degree to which the π_2 mode was detected varied greatly: π_2 was detected for all q for the (15,1)

272 tube, only for $q \geq 0.72 \, \text{Å}^{-1}$ for the (15,10), and, not at all for the (13,7) tube.

273 Using a purpose-built stand-alone EEL spectrometer apparatus,[50] a π peak splitting has been identified in

274 measurements averaged over "bulk samples" containing a large number of bundles of aligned SWCNTs.[6-8]

275 Kramberger et al.[6, 7] and Liu et al.[8] reported interpretations of the SWCNT π plasmon EEL peak splitting in

276 terms of polarisation-dependent plasmon confinement. This suggests that the non-dispersive π_1 mode

277 corresponds to π plasmon confinement perpendicular to SWCNT axis while the prominent dispersion of the π_2

278 mode indicates significant plasmon propagation along the SWCNT axis. While the π_1 mode was not identified

279 by Pichler et al.[5] and Knupfer et al.,[49] they too attributed the significant dispersion of the π_2 mode to

280 polarisation-dependent plasmon propagation along the CNT axes. This interpretation can be illustrated

281 conceptually by considering a plasmon as the quasi-particle corresponding to envelopes over the collective

282 valence electron oscillations set up by the impinging electron beam.[32] From the definition of the group velocity,

283 the dispersion of the plasmon indicates the degree to which it is allowed to propagate in the system: a non-

284 dispersive plasmon indicates zero group velocity (*i.e.* a standing wave) and thus a localised mode, while a

285 dispersive mode indicates a non-zero group velocity and thus significant plasmon propagation.[27] For detailed

286 analysis of SWCNT π and $\pi+\sigma$ plasmon dispersions, local field effects (LFEs) need to be considered.

287 Kramberger et al.[6] showed by means of *ab initio* modelling and momentum resolved EEL spectra that LFEs are

288 of major importance for the π plasmon dispersion of SWCNTs (as well as for mono and bi-layer graphene). The

289 contribution of LFEs was attributed to the observed and predicted SWCNT π plasmon dispersions deviating

290 significantly from that of graphite and bundled SWCNTs.

291 In order to accurately interpret the observed differences in π_2 plasmon dispersion between the three tubes (Figs.

292 5-7), the experimental setup and direction momentum selectivity must first be taken into consideration. The

293 reported[8] and inferred[5-7, 49] π plasmon polarisation dependence means the π_1 mode will appear at the highest

294 relative intensity for spectra formed by collecting electrons that have imparted momentum to the sample valence

295 π electrons perpendicular to the nanotube axis. Conversely, the π_2 mode will appear at the highest relative

296 intensity for spectra formed by collecting electrons that have imparted momentum to the sample valence π

297 electrons parallel to the nanotube axis. The relative orientation of the momentum selecting slit to the tubes' axial

298 directions is indicated schematically in the diffraction patterns in Fig. 1, which gives the direction of q for each

299 measured tube (indicated in Fig. 1). This schematic demonstrates that if the π_2 mode response of all three tubes

300 was identical, experimental geometry alone would dictate that the relative intensity of the π_2 mode would

301 increase from the (15,1) tube to the (15,10) tube and be at its highest relative intensity for the (13,7) tube.

302 However, the spectra in Figs. 5 and 6 show clearly that this is not the case. Hence the results shown in Figs. 5-7

303 cannot be explained in terms of experimental geometry alone.

304 The observed differences in π_2 plasmon dispersion might rather be understood in terms of variable

305 topologically-induced plasmon confinement along the nanotube axis. Specifically, it is postulated that the degree

306 to which the π_2 mode is confined (along the tube axis) depends on the concentration of topological defects (*i.e.*

11

307 non-hexagonal rings) in a SWCNT. From comparing the MAADF images in Fig. 1 and the dispersions in Fig. 7,

308 it can be deduced that the π_2 mode is: significantly confined at all probed wavelengths (*i.e.* all values of q) in the

309 tube containing the largest number of topological defects (13,7); confined only at longer wavelengths

310 $\left(q < \approx 0.7\,\text{Å}^{-1} \right)$ for the tube containing an intermediate number of defects (15,10); and allowed to propagate in

311 the range of all measured wavelengths for the least defective tube (15,1). This is consistent with a negligible

312 effect of tube defects on π_2 plasmon propagation in the (15,1) tube. A topologically-induced π_2 mode

313 confinement can be viewed as similar to the confinement of the π_1 mode perpendicular to the tube axis (induced

314 by the finite diameter of the nanotube itself). The above interpretation is in good agreement with the reported

315 identification of topologically induced π plasmon confinement at the tip of a multi-layered graphene cone.[27] One

316 might argue that intrinsic structural periodicity along the CNT axis might also impose collective mode

317 confinement in the system. The lattice parameters in the axial direction are (13,7): 25 Å, (15,1): 66 Å and

318 (15,10): 19 Å, which gives first Brillouin Zone boundaries (13,7): 0.13 Å^{-1}, (15,1): 0.05 Å^{-1} and (15,10): 0.17 Å^{-1}

319 . From comparing theses values to the dispersions in Fig. 7 it is clear that there is no obvious relationship

320 between intrinsic structural periodicity along the CNT axis and the observed degree of π_2 plasmon confinement.

321 Thus in the present case, π_2 mode confinement is attributed solely to the concentration of topological defects

322 incorporated in the CNT walls. Conceptually, this might be understood as non-hexagonal rings in the CNT walls

323 disrupting the delocalised π states in the tube walls, which in turn disrupts π plasmon propagation along the tube

324 axis.

325 Note that for the (15, 1) tube, the apparent difference between the π_1 and π_2 peak energies in the "$q \rightarrow 0$

326 spectrum" (Figs. 5-7) can be explained by experimental geometry, rather than being interpreted as a result of

327 confinement. Due to a very modest momentum resolution ($\pm$ 0.25 Å^{-1}), all momentum resolved spectra in the

328 present work include significant contributions from a range of momentum transfers. Hence the (15, 1) tube

329 "$q \rightarrow 0$ spectrum" will include contributions from the dispersive π_2 mode for q up to $\approx$ 0.25 Å^{-1}. This effectively

330 blue-shifts the π_2 plasmon peak by an amount dependent on momentum resolution (*i.e.* beam convergence and

331 effective size of spectrometer collection aperture). As the π_1 mode is non-dispersive, no comparable shift is

332 expected for the π_1 peak. Thus experimental geometry in combination with differences between π_1 and π_2 mode

333 dispersions can be used to rationalise the measured energy difference between the π_1 and π_2 peaks in the "$q \rightarrow 0$

334 spectrum" of the (15, 1) tube (Figs. 5-7).

335   In contrast, no significant differences were found between the tubes in terms of $\pi+\sigma$ or IB peak dispersions (see

336   Figs. 5-7). Kramberger et al.[6, 7] reported a $\pi+\sigma$ peak split into a dispersive and non-dispersive mode for "bulk"

337   samples of aligned tubes. As for the π plasmon, they attributed the non-dispersive nature of the $\pi+\sigma$ mode to

338   confinement perpendicular to the nanotube axis. While due to spectral noise, a $\pi+\sigma$ peak split could not be

339   unambiguously identified over the whole range of q values, the asymmetry of the $\pi+\sigma$ peak of the (15,10) and

340   (15,1) spectra at high q in Fig. 5 appears very consistent with the result of Kramberger et al.[6, 7] In light of the

341   above discussion on the π_2 mode confinement, the $\pi+\sigma$ peak might then be expected to be show non-dispersive

342   behaviour for the (13,7) tube. Indeed, such an effect is observed for C_{60}[51] as well as at the tip of a multilayer

343   graphene cone.[27] However, no localisation of the $\pi+\sigma$ mode along the tube axis is apparent for the (13,7)

344   SWCNT in Figs. 5 and 7. Thus it must be concluded that topologically-induced confinement primarily affects

345   the π plasmon in the SWCNTs investigated in the present work. CNT σ states are significantly more localised

346   than π states, which might explain the apparent difference in $\pi+\sigma$ and π plasmon response to the presence of

347   non-hexagonal rings incorporated in the CNT wall, at least in part. In–depth analysis of the measured π and $\pi+\sigma$

348   plasmon dispersions might shed further light on the relative contributions of topological defects and chirality

349   dependent band structure. Due to the significant contribution of LFEs in the investigated systems,[6] such a study

350   would likely require comprehensive *ab into* modelling. It might also be of significant interest to investigate in

351   future work the degree to which topological defects affect the propagation of the free charge carrier plasmon

352   along the tube axis.

353   From the above discussion it is clear that topological defects significantly affect the plasmonic performance of

354   SWCNTs. By extension, topological defects might thus affect the plasmonic response of graphene in a similar

355   manner. As both CNTs and graphene are currently of significant interest for the development of plasmonic and

356   opto-electronic devices,[46] the presence of topological defects might therefore be important to take into

357   consideration in future developments in this field. Furthermore, it is suggested that by accurate and deliberate

358   introduction of topological defects, the propagation of the π plasmon could be tailored in such a fashion as to

359   form plasmonic conduits or "wires" and even more complex functional geometries.

360   **D. Spatially resolved valence loss spectra**

361   Returning to a more conventional STEM-EELS approach, the spatially-resolved valence loss spectra of (15,10),

362   (15,1) and (13,7) tubes are shown in Fig. 8 as a function of impact parameter (b). The experimental procedure is

363   indicated in the MAADF image of the (15, 1) tube in Fig. 1; the electron beam is moved progressively from the

364   centre of the tube (b = 0 nm) indicated by the white discs (Fig. 1.), past the tube wall (b = 0.5-1nm) and into

365   vacuum $\left(b > \sim 1\text{nm} \right)$ with increasing distance to the tube centre (*i.e.* increasing b). Overall, loss peak intensities

366   decrease with increasing impact parameter for all three tubes, in agreement with the literature.[38, 52, 53] In a

367   classical particle description, the maximum impact parameter allowed (in the adiabatic limit) can be expressed

368   as $b_{max} = v_0 / (E / \hbar)$, where E is the energy loss and v_0 is the (relativistic) velocity of the impinging

369   electron.[32] The possibility to excite a mode at a given E for an impact parameter up to b_{max}, is often referred to as

370   *inelastic delocalisation.* Effectively, a loss peak at a certain E will decrease more in intensity with increasing b

371   than a lower energy peak,[32] as is the trend for all three tube spectra in Fig. 8.

372   For the (13,7) tube, a ≈ 5.5 eV peak on the high energy shoulder of the π plasmon peak appears to increase from

373   the tube centre (b = 0 nm) to the tube wall (b = 0.5-1.0 nm). For $b > \sim 1 \text{ nm}$, qualitatively the ≈ 5.5 eV peak

374   decreases in intensity along with the rest of the peaks in the spectrum in agreement with inelastic scattering

375   theory, discussed above. To understand the relative increase in ≈ 5.5 eV peak intensity from b = 0 nm to b =

376   0.5-1.0 nm, both experimental geometry and π_2 mode dispersion need to be taken into consideration. For the

377   (15,1) and (15,10) tubes the higher energy shoulder of their respective π peaks can be attributed to the π_2 mode.

378   As discussed above, due to the use of finite beam convergence and spectrometer collection angles (see section

379   II), higher q components of the π_2 mode contribute to the recorded spectrum, resulting in an apparent blue-shift

380   of the π_2 mode, with respect to the "π peak". As the π_2 mode can be attributed to the tangential tube response,[38]

381   the observed gradual decrease of the (15,1) and (15,10) "π_2 shoulder" intensities with increasing b is as expected

382   from inelastic scattering theory.

383   However, as no dispersive π_2 mode was observed for the (13,7) tube (see Figs. 5-7), the presence of the ≈ 5.5 eV

384   peak must be understood in terms of experimental geometry. Due to a finite beam convergence and spectrometer

385   collection aperture (see section II) the EEL spectrum is dominated by electrons having undergone momentum

386   transfer perpendicular to the incident beam direction. Thus when the electron beam is incident on the nanotube

387   axis (b = 0 nm) the spectrum is dominated by the CNT tangential response. However, when the beam is moved

388   to the wall of the nanotube (b = 0.5-1.0nm), the relative radial contribution increases significantly. As the ≈ 5.5

389   eV peak increases significantly in intensity from b = 0 nm to b = 0.5-1.0 nm for the (13,7) tube, the peak is

390   tentatively attributed to a chirality dependent interband transition associated with the radial response of the

391   (13,7) SWCNT. Being attributed to the radial rather than the tangential response, clearly differentiates the (13,7)

392   ≈ 5.5 eV peak from the "π_2 mode shoulders" of the (15,1) and (15,10) tubes in Fig. 8. A more accurate mode

393   assignment of the $(13,7) \approx 5.5$ eV peak might result from theoretical modelling, possibly requiring the inclusion

394   of depolarisation and excitonic effects. This is however beyond the scope of the present work.

395   In light of the above discussion, a significant reduction in the high energy shoulder of the $\pi+\sigma$ peak with

396   increasing b for all three tubes might also be understood in terms of experimental geometry and loss mode

397   dispersion. For $b = 0$ nm the $\pi+\sigma$ peak results from the spectrometer accepting electrons that have undergone a

398   range of momentum transfers, beyond the first Brillouin zone. As the $\pi+\sigma$ mode is dispersive (see Fig. 8), it

399   follows that the corresponding loss peak is effectively broadened on the high energy loss side by the higher q

400   contributions of the $\pi+\sigma$ response. With increasing b the relative magnitude of q of the tangential tube response

401   contributing to the collected spectrum decreases. As the SWCNTs $\pi+\sigma$ mode is tangential,[38] the contribution of

402   the high q components of the $\pi+\sigma$ mode to the recorded loss peak decreases with increasing b. Thus, the

403   broadening of the $\pi+\sigma$ peak is reduced with increasing b for SWCNTs. This result clearly shows that a coherent

404   interpretation of the spatially resolved spectra results in Fig. 8 not only requires knowledge of sample

405   orientation and experimental parameters but also of the momentum dependence of the SWCNT loss modes

406   themselves. In extension, similar considerations might prove useful when using valence EELS to studying other

407   low-dimensional and anisotropic samples.

408

409   **IV. CONCLUSION**

410   STEM-EELS allows for a flexible and comprehensive characterisation of the electronic structure of individual

411   SWCNTs. Information that can be obtained includes: chiral indices and structure, identification of topological

412   defects and disordered carbonaceous material coverage (and their effect on EEL spectra), chirality-dependent

413   interband transition energies and C-K ionisation edge fine structure, and, determination of plasmon and

414   interband transition peak dispersions. The energy resolution provided by state-of-the-art STEM

415   monochromators allows for spectral analysis of electronic structure comparable to that of many optical methods

416   and dedicated EEL spectrometers. But crucially, STEM-EELS allows for the investigation of <u>individual</u> tubes

417   and their defects, which is information that to a large degree is obscured in results from many optical

418   spectroscopic methods and dedicated EEL spectrometers. In order to achieve the spatial resolution necessary to

419   identify individual SWCNTs, the momentum resolution in the present work is significantly poorer than that

420   offered by stand-alone dedicated spectrometers. However, due to the highly flexible optics of the electron

421   microscope the intrinsic trade-off between spatial and momentum resolution can be optimised for a given

422 experiment. Thus the momentum resolution could be made to approach that of dedicated spectrometers, if

423 required.

424 The present results highlight the advantages of combining information from spatially- and momentum-resolved

425 measurements when evaluating the effects of nanotube defects and chirality. Moreover, a careful comparison of

426 spatially- and momentum-resolved spectra from the same nano-object emphasises how the relative sample

427 orientation and choice of experimental parameters along with the dispersions of relevant loss modes might

428 significantly affect valence EEL spectra of SWCNTs. The degree of π plasmon confinement parallel to the

429 SWCNT axis was shown to be dependent on the local concentration of topological defects. While the exact

430 mechanism for confinement remains unclear, this suggests that the plasmonic response of SWCNTs could be

431 tailored by accurate control of the topological defect concentration. By extension, a similar degree of tailoring

432 might be possible for graphene with the aim to create plasmonic conduits or "wires" and even more complex

433 functional geometries. Thus accurate control of the plasmonic response through the use of topological defects

434 might prove to be beneficial in the development of SWCNTs or graphene based novel plasmonic and opto-

435 electronic devices.

References

443   1   S. Iijima, Nature **354**, 56 (1991).
444   2   R. Saito, M. Fujita, G. Dresselhaus, and M. S. Dresselhaus, Physical Review B **46**, 1804 (1992).
445   3   N. Hamada, S.-i. Sawada, and A. Oshiyama, Physical Review Letters **68**, 1579 (1992).
446   4   B. J. LeRoy, S. G. Lemay, J. Kong, and C. Dekker, Applied Physics Letters **84**, 4280 (2004).
447   5   T. Pichler, M. Knupfer, M. S. Golden, J. Fink, A. Rinzler, and R. E. Smalley, Physical Review
448   Letters **80**, 4729 (1998).
449   6   C. Kramberger, R. Hambach, C. Giorgetti, M. H. Rümmeli, M. Knupfer, J. Fink, B. Büchner, L.
450   Reining, E. Einarsson, S. Maruyama, F. Sottile, K. Hannewald, V. Olevano, A. G.
451   Marinopoulos, and T. Pichler, Physical Review Letters **100**, 196803 (2008).
452   7   C. Kramberger, T. Thurakitseree, S. Maruyama, and M. Knupfer, Nanotechnology **24**, 405202
453   (2013).
454   8   X. Liu, T. Pichler, M. Knupfer, M. S. Golden, J. Fink, D. A. Walters, M. J. Casavant, J. Schmidt,
455   and R. E. Smalley, Synthetic Metals **121**, 1183 (2001).
456   9   K. Liu, J. Deslippe, F. Xiao, R. B. Capaz, X. Hong, S. Aloni, A. Zettl, W. Wang, X. Bai, S. G. Louie,
457   E. Wang, and F. Wang, Nature Nanotechnology **7**, 325 (2012).
458   10 M. Y. Sfeir, T. Beetz, F. Wang, L. Huang, X. M. H. Huang, M. Huang, J. Hone, S. Brien, J. A.
459   Misewich, T. F. Heinz, L. Wu, Y. Zhu, and L. E. Brus, Science **312**, 554 (2006).
460   11 S. M. Bachilo, M. S. Strano, C. Kittrell, R. H. Hauge, R. E. Smalley, and R. B. Weisman, Science
461   **298**, 2361 (2002).
462   12 A. Roch, L. Stepien, T. Roch, I. Dani, C. Leyens, O. Jost, and A. Leson, Synthetic Metals **197**,
463   182 (2014).
464   13 J.-C. Blancon, M. Paillet, H. N. Tran, X. T. Than, S. A. Guebrou, A. Ayari, A. S. Miguel, N.-M.
465   Phan, A.-A. Zahab, J.-L. Sauvajol, N. D. Fatti, and F. Vallée, Nature Communications **4**, 2542
466   (2013).
467   14 D. Christofilos, J. C. Blancon, J. Arvanitidis, A. S. Miguel, A. Ayari, N. Del Fatti, and F. Vallée,
468   The Journal of Physical Chemistry Letters **3**, 1176 (2012).
469   15 O. L. Krivanek, J. P. Ursin, N. J. Bacon, G. J. Corbin, N. Dellby, P. Hrncirik, M. F. Murfitt, C. S.
470   Own, and Z. S. Szilagyi, Philosophical Transactions of the Royal Society A: Mathematical,
471   Physical and Engineering Sciences **367**, 3683 (2009).
472   16 O. L. Krivanek, T. C. Lovejoy, N. Dellby, T. Aoki, R. W. Carpenter, P. Rez, E. Soignard, J. Zhu, P.
473   E. Batson, M. J. Lagos, R. F. Egerton, and P. A. Crozier, Nature **514**, 209 (2014).
474   17 M. Mukai, J. S. Kim, K. Omoto, H. Sawada, A. Kimura, A. Ikeda, J. Zhou, T. Kaneyama, N. P.
475   Young, J. H. Warner, P. D. Nellist, and A. I. Kirkland, Ultramicroscopy **140**, 37 (2014).
476   18 Y. Sato and M. Terauchi, Microscopy and Microanalysis **20**, 807 (2014).
477   19 R. Senga, T. Pichler, and K. Suenaga, Nano Letters **16**, 3661 (2016).
478   20 H. Zhu, K. Suenaga, A. Hashimoto, K. Urita, and S. Iijima, Chemical Physics Letters **412**, 116
479   (2005).
480   21 M. Gao, J. M. Zuo, R. D. Twesten, I. Petrov, L. A. Nagahara, and R. Zhang, Applied Physics
481   Letters **82**, 2703 (2003).
482   22 L.-C. Qin, Physical Chemistry Chemical Physics **9**, 31 (2007).
483   23 R. Saito, G. Dresselhaus, and M. S. Dresselhaus, Physical Review B **61**, 2981 (2000).
484   24 M. K. Kinyanjui, C. Kramberger, T. Pichler, J. C. Meyer, P. Wachsmuth, G. Benner, and U.
485   Kaiser, Europhysics Letters **97**, 57005 (2012).
486   25 P. Wachsmuth, R. Hambach, M. K. Kinyanjui, M. Guzzo, G. Benner, and U. Kaiser, Physical
487   Review B **88**, 075433 (2013).
488   26 S. C. Liou, C. S. Shie, C. H. Chen, R. Breitwieser, W. W. Pai, G. Y. Guo, and M. W. Chu, Physical
489   Review B **91**, 045418 (2015).
490   27 F. S. Hage, Q. M. Ramasse, D. M. Kepaptsoglou, Ø. Prytz, A. E. Gunnaes, G. Helgesen, and R.
491   Brydson, Physical Review B **88**, 155408 (2013).

492 28 E. Najafi, A. P. Hitchcock, D. Rossouw, and G. A. Botton, Ultramicroscopy **113**, 158 (2012).

493 29 U. Falke, A.-K. Weber, and J. Ullmann, Microsc. Microanal. Microstruct. **6**, 113 (1995).

494 30 R. Saito, M. Fujita, G. Dresselhaus, and M. S. Dresselhaus, Applied Physics Letters **60**, 2204
495 (1992).

496 31 D. Rossouw, G. A. Botton, E. Najafi, V. Lee, and A. P. Hitchcock, ACS Nano **6**, 10965 (2012).

497 32 R. F. Egerton, *Electron Energy-Loss Spectroscopy in the Electron Microscope* (Springer US,
498 2011).

499 33 K. Suenaga and M. Koshino, Nature **468**, 1088 (2010).

500 34 R. B. Weisman and S. M. Bachilo, Nano Letters **3**, 1235 (2003).

501 35 A. G. Marinopoulos, L. Reining, A. Rubio, and V. Olevano, Physical Review B **69**, 245419
502 (2004).

503 36 D. Novko, V. Despoja, and M. Šunjić, Physical Review B **91**, 195407 (2015).

504 37 E. Malić, M. Hirtschulz, F. Milde, Y. Wu, J. Maultzsch, T. F. Heinz, A. Knorr, and S. Reich,
505 Physical Review B **77**, 045432 (2008).

506 38 O. Stéphan, D. Taverna, M. Kociak, K. Suenaga, L. Henrard, and C. Colliex, Physical Review B
507 **66**, 155422 (2002).

508 39 H. Raether, *Excitations of Plasmons and Interband Transitions by Electrons* (Springer-Verlag,
509 New York, 1980).

510 40 A. G. Marinopoulos, L. Reining, and A. Rubio, Physical Review B **78**, 235428 (2008).

511 41 F. Bassani and G. Pastori Parravicini, Il Nuovo Cimento B (1965-1970) **50**, 95 (1967).

512 42 H. Daniels, R. Brydson, B. Rand, and A. Brown, Philosophical Magazine **87**, 4073 (2007).

513 43 F. S. Hage, D. M. Kepaptsoglou, C. R. Seabourne, Q. M. Ramasse, A. J. Scott, O. Prytz, A. E.
514 Gunnaes, and G. Helgesen, Nanoscale **6**, 1833 (2014).

515 44 T. Stockli, J.-M. Bonard, A. Chatelain, Z. L. Wang, and P. Stadelmann, Applied Physics Letters
516 **80**, 2982 (2002).

517 45 W. Zhou, J. Lee, J. Nanda, S. T. Pantelides, S. J. Pennycook, and J.-C. Idrobo, Nat Nano **7**, 161
518 (2012).

519 46 F. J. García de Abajo, ACS Photonics **1**, 135 (2014).

520 47 Q. Zhang, E. H. Hároz, Z. Jin, L. Ren, X. Wang, R. S. Arvidson, A. Lüttge, and J. Kono, Nano
521 Letters **13**, 5991 (2013).

522 48 T. Morimoto, S.-K. Joung, T. Saito, D. N. Futaba, K. Hata, and T. Okazaki, ACS Nano **8**, 9897
523 (2014).

524 49 M. Knupfer, T. Pichler, M. S. Golden, J. Fink, A. Rinzler, and R. E. Smalley, Carbon **37**, 733
525 (1999).

526 50 J. Fink, in *Advances in Electronics and Electron Physics* (Academic Press, London, 1989), p.
527 121.

528 51 T. Pichler, M. Knupfer, M. S. Golden, J. Fink, and T. Cabioc'h, Physical Review B **63**, 155415
529 (2001).

530 52 B. W. Reed and M. Sarikaya, Physical Review B **64**, 195404 (2001).

531 53 M. Kociak, L. Henrard, O. Stéphan, K. Suenaga, and C. Colliex, Physical Review B **61**, 13936
532 (2000).

533
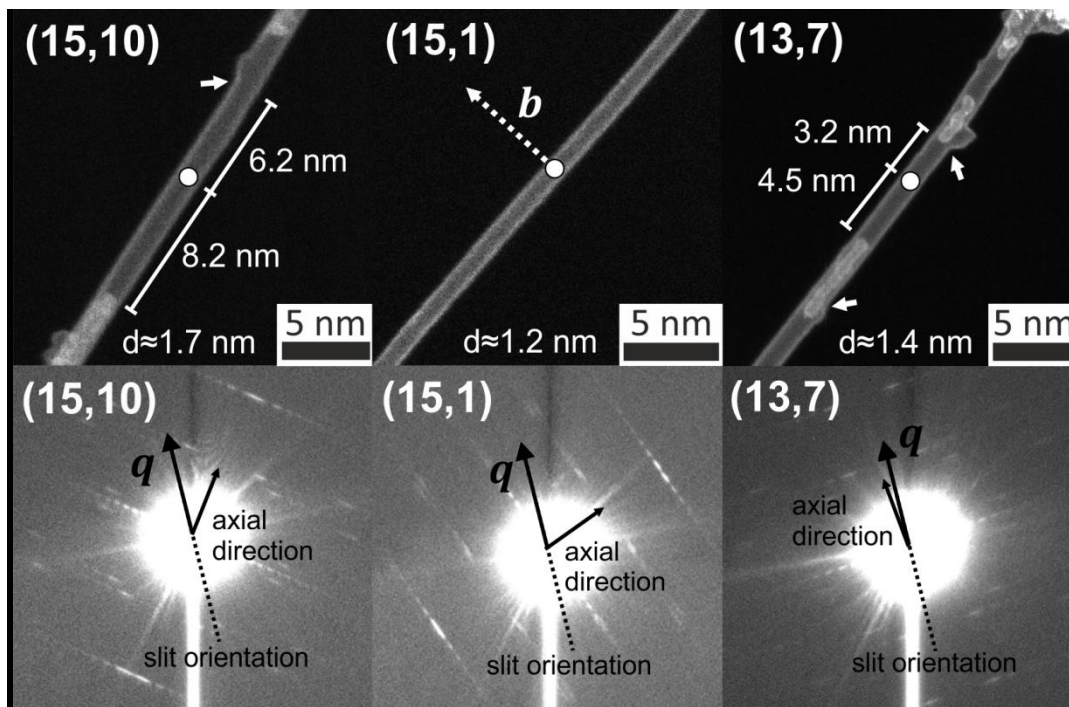
FIG. 1. MAADF images and diffraction patterns of three SWCNTs. Topological defects in the (15,10) and (13,7) tubes are indicated by white arrows. The momentum-selecting slit orientations and the tube axis directions are indicated in the diffraction patterns. The orientation of the tubes in the MAADF images is not directly related to the orientations of the diffraction patterns. The white discs superimposed on the MAADF images indicate the beam potions at which the spectra in Fig. 3 were acquired. The white lines superimposed on the MAADF images indicate the distance between the beam positions (white discs) and tube defects. The dashed white arrow in the (15,1) tube MAADF image illustrates the experimental setup used to acquire the spectra shown in Fig. 8.
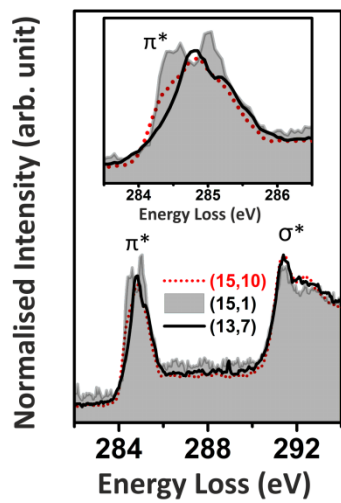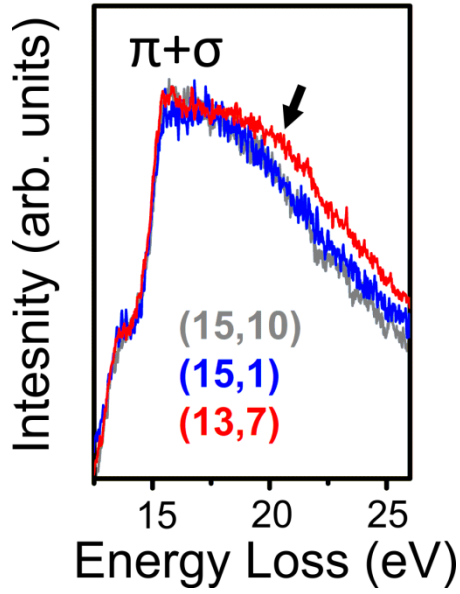
543

544   FIG. 2. Core loss C-*K* edges from the SWCNTs.

545
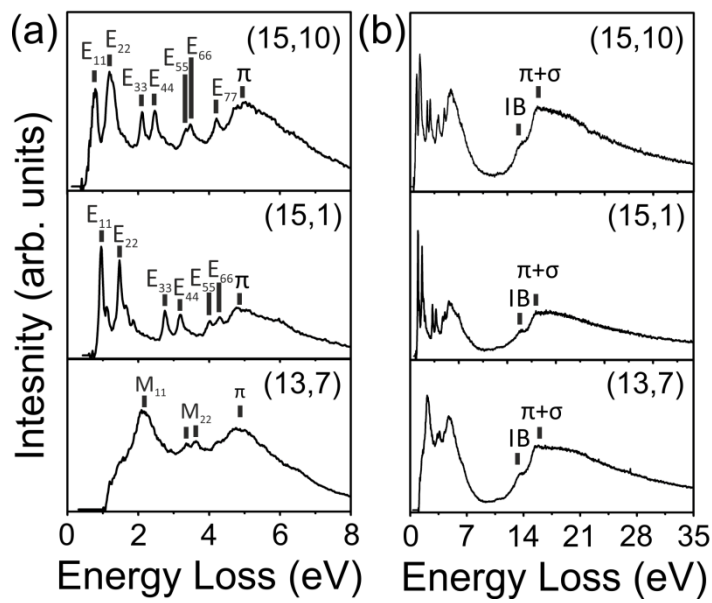
FIG. 3. Valence loss spectra from the three tubes.

FIG. 4. Comparison of the π+σ plasmon peaks from the three tubes. The black arrow indicates the spectral contribution of disordered carbonaceous material deposited on or inside the (13,7) tube.

TABLE I. Experimental SWCNT structural parameters determined from the diffraction patterns in Fig. 1 (exp.) compared to the predicted values.[22]

Nanotube	Chiral angle (°)	m/n	X_2/X_1	m (X_2/X_1) [22]
(15,10) exp. (Ref. [22])	24 (23.413)	0.7 (0.667)	1.41	10 (1.398) or 9 (1.428)
(15,1) exp. (Ref. [22])	2 (3.192)	0.04 (0.0667)	2.89	1 (2.892)
(13,7) exp. (Ref. [22])	21 (20.174)	0.6 (0.5385)	1.48	7 (1.507) or 8 (1.465)

557

TABLE II. Measured $\pi \rightarrow \pi^*$ "vHs peak" values for the (15,10) and (15,1) tubes, compared to reported values from Rayleigh scattering spectroscopy,[9, 10] fluorescence excitation spectroscopy,[11] optical absorption spectroscopy[12] and empirical prediction based on florescence data.[34]

| Semiconducting	E_{11} (eV)	E_{22} (eV)	E_{33} (eV)	E_{44} (eV)
(15,10) EELS	0.79	1.22	2.11	2.47
(15,10)	0.624 (Ref. [34])	1.072 (Ref. [34])	2.13, 2.15 (Refs. [9, 10])	2.41, 2.44 (Refs. [9, 10])
(15,1) EELS	0.97	1.48	2.76	3.19
(15,1) (Refs. [11, 12, 34])	0.870, 0.848, 0.869	1.337, 1.379, 1.347	n/a	n/a

561

562

TABLE III. Measured $\pi \rightarrow \pi^*$ "vHs peak" values for the (13,7) tube, compared to values interpolated from experimental optical data [9] and optical absorption spectroscopy.[12]

| Metallic	$M_{11}^{\pm}$ (eV)	$M_{22}^{\pm}$ (eV)
(13,7) EELS	2.15	3.30 (-) 3.61 (+)
(13,7) (Refs. [9, 12])	1.81 (-) 1.96 (+), 1.857(-) 1.984 (+)	n/a

565
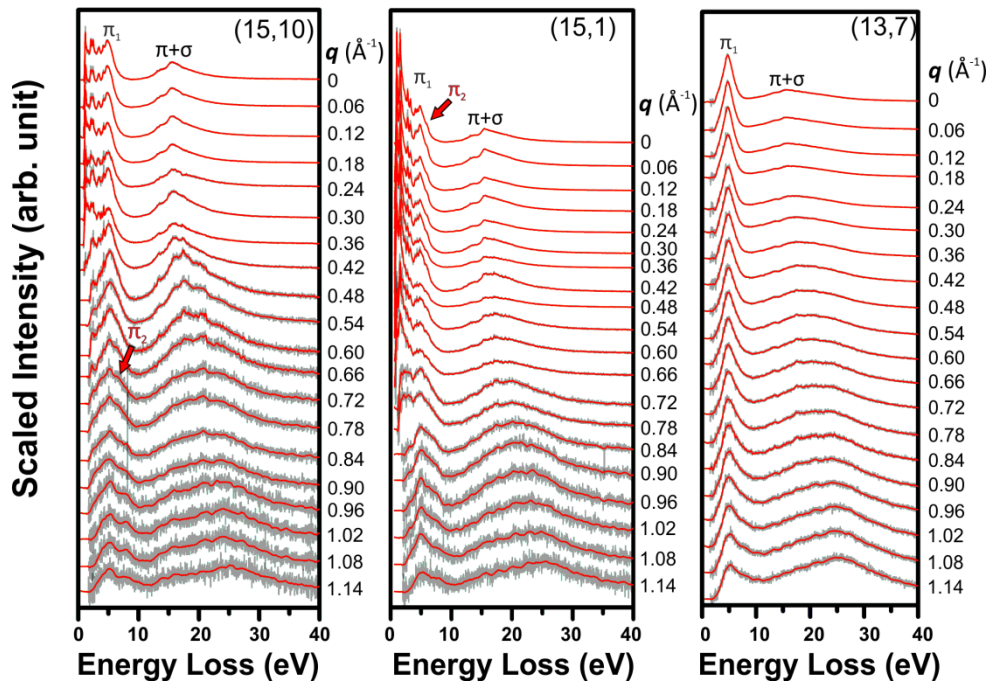
FIG. 5. ZLP-subtracted momentum-resolved valence loss spectra of the SWCNTs. Smoothed data (red) super imposed on the raw data (grey) as a guide to the eye. Spectral intensities are scaled for ease of comparison. The direction of *q* with respect to the CNT axial direction for each tube is indicated in the diffraction patterns in Fig. 1.

572
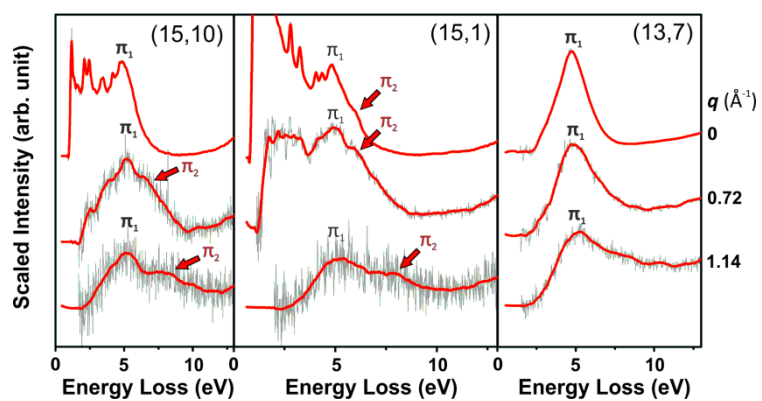
573

574 FIG. 6. Selected momentum-resolved valence loss spectra of the SWCNTs. Smoothed data (red) superimposed
575 on the raw data (grey) as a guide to the eye. Spectral intensities are scaled for ease of comparison. The direction
576 of q with respect to the CNT axial direction for each tube is indicated in the diffraction patterns in Fig. 1.
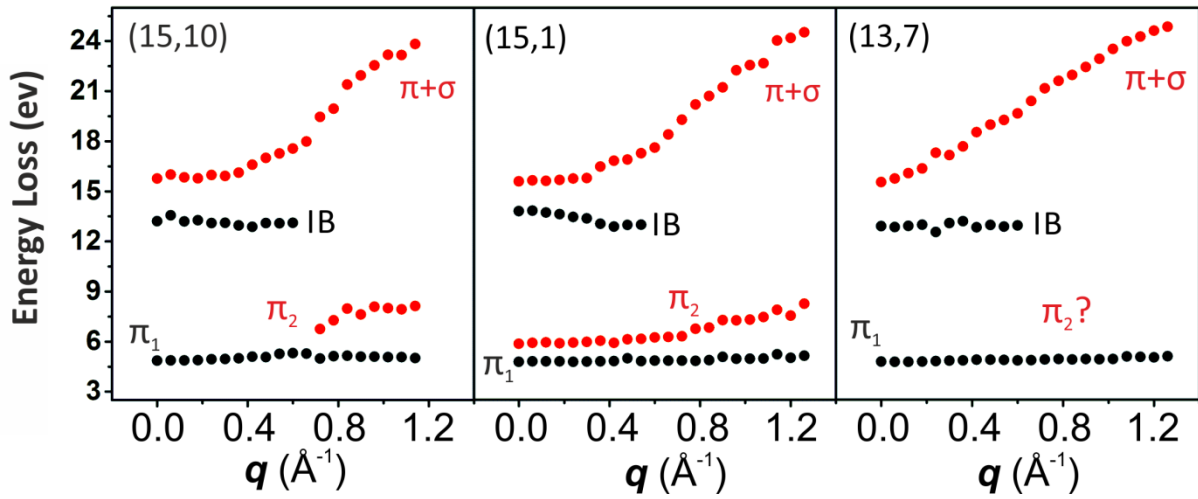
FIG. 7. SWCNT valence loss peak dispersions. Errors in energy loss peak positions are estimated to range from $< \pm 0.02$ eV at low q to a maximum of $\sim \pm 0.2$ eV for the highest q measurements. The momentum resolution is estimated to $\Delta q \approx \pm 0.25$ Å^{-1}. The direction of q with respect to the CNT axial direction for each tube is indicated in the diffraction patterns in Fig. 1.
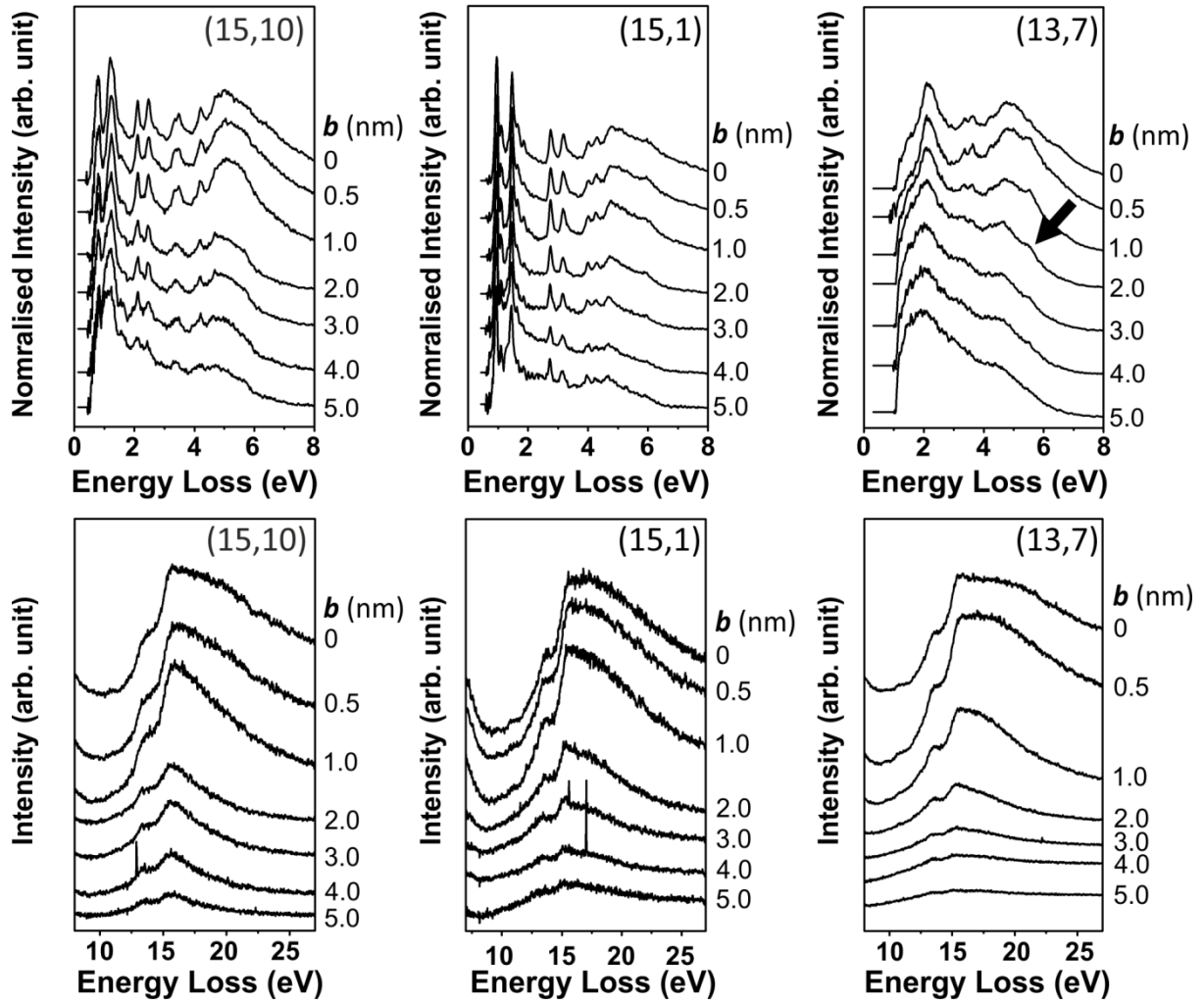
FIG. 8. Spatially-resolved valence loss spectra as a function of impact parameter. The black arrow indicates a chirality-dependent radial interband transition.